Landslides
DOI 10.1007/s10346-025-02509-8
Received: 11 November 2024
Accepted: 14 March 2025

Luigi Guerriero · Rita Tufano · Vincenzo Capozzi · Giorgio Budillon · Chiara Di Muro · Lorenzo Esposito · Giovanni Forte · Enza Vitale · Domenico Calcaterra

A postwildfire debris flood in Gragnano, southern Italy, on September 11, 2024

Abstract On September 11, 2024, a debris flood hit the urban area of Gragnano (in Naples) in the Lattari Mts. of southern Italy and resulted in the evacuation of nine families. This event was triggered by a storm that occurred 1 month after a wildfire affected two catchments located along the northern slopes of Mt. Pendolo. The increasing frequency of debris floods in peri-Vesuvian areas and effects of this event led to this analysis. In this study, we analyze the event and assess its magnitude and conditions of development in relation to the preceding wildfire. Field observations were supported by unmanned aerial vehicle (UAV)-aided photography, LiDAR data acquisition, digital elevation models (DEMs), and satellite imagery interpretation. Rainfall data and runoff modeling were also used. The results indicated that (i) the wildfire affected two catchments of 0.041 km^2 and 0.075 km^2 that contributed sediment to the debris flood, (ii) the wildfire severity ranged from moderate to moderate–high, (iii) the triggering rainfall produced a total of 24.7 mm of rain over a duration of 80 min, (iv) the sediment transported by the event contained mostly pumices, (v) the inundation area corresponded primarily to major roads and extended for a total of 0.05 km^2, (vi) the total gross sediment volume entrained into the flow was estimated to be ~ 4100 m^3, and (vii) the clear-water peak discharge was estimated to be 4.6 m^3/s for the eastern catchment and 2.7 m^3/s for the western catchment. These results provide a better understanding of events that are becoming increasingly frequent with ongoing climate change.

Keywords Debris flood · Pyroclastic deposits · Rainfall · Peak discharge · Lattari Mts

Introduction

On August 11, 2024, a wildfire on the northeastern slope of Mt. Pendolo, Italy, devastated vegetation and threatened multiple buildings (Fig. 1a). One month later, on September 11, 2024, a storm triggered a debris flood (sensu Hungr et al. 2014) that affected the urban area of Gragnano in the province of Naples (southern Italy) and resulted in the evacuation of nine families (Fig. 1b–d). This event was the most recent of a series of significant events that have impacted the slopes of this relief. For example, in 1997, the western slope of Mt. Pendolo was affected by a debris flow that caused the death of livestock. In 1971, a landslide along the same mountainside destroyed buildings and caused the loss of six lives. In 1963, several landslides triggered by storms damaged the urban area of Gragnano. Landslides in 1841 and 1764 also damaged settlements and claimed victims (Mele and Del Prete 1999; de Riso et al. 2004). The frequency of debris flows, debris floods, and debris avalanches (sensu Hungr et al. 2014) in this area is related to the geological setting and, in particular, to pyroclastic soils resting on steep bedrock (e.g., Revellino et al. 2013; Sepe et al. 2023a). In other areas of the Campania region, the presence of pyroclastic soils on a different type of bedrock (flyschoid) also predisposes the slopes to debris slides (e.g., Guerriero et al. 2019). This geological condition is typical of the Lattari Mts., which have experienced many landslides. The earliest records of landslides in this area date to 1910 and 1954, when intense rainfall triggered hundreds of debris flows and debris floods. Additional events occurred between the 1950s and 1990s (Calcaterra and Santo 2004; Forte et al. 2019; Santangelo et al. 2021).

Debris floods in burned basins have been observed in several regions of the world and are prevalent in the western USA and southern Europe (e.g., Cannon et al.1998; Gabet and Bookter 2008; Calcaterra et al. 2007; Cannon et al. 2010; Carabella et al. 2019; Guerriero et al. 2024). They originate in steep channels from runoff-dominated erosion, debris flow dilution, or floods from artificial or natural dams when the streambed becomes mobile (Church and Jakob 2020). Sediment availability for debris flood development is generally related to hillslope-divergent and hillslope-convergent processes. Raindrop impact-induced erosion, ravel, surface washing, and rilling are the primary erosional processes that initiate postwildfire events (Staley et al. 2013). The removal of soil-mantling vegetation and litter caused by wildfires, the deposition of ash, changes in the physical properties of soils and rocks, and the generation or destruction of water-repellent soils can increase sediment availability and surface runoff (Parise and Cannon 2012). The timing and magnitude of surface runoff-initiated debris floods are consistently related to local peaks in short-duration rainfalls that induce a fast response in the channel flow stage (a few minutes to a few hours, Kean et al. 2011; Borga et al. 2014).

The number and severity of wildfires are increasing worldwide due to ongoing climate change and increased human pressure, and in recent decades, the frequency and magnitude of postwildfire debris floods have increased, as have their impacts on settlements and human life. In this paper, we analyze a debris flood that occurred in Gragnano, Italy, on September 11, 2024, as well as the role that wildfire played in the debris flood. The extent and severity of the preceding wildfire were evaluated using prefire and postfire Sentinel-2 satellite imagery, and the characteristics of the rainfall that triggered the debris flood were analyzed using available meteorological data. The magnitude and impact of the debris flood in terms of the peak discharge, sediment budget, and inundation area were subsequently evaluated using rainfall data, field observations, and analysis of digital elevation models (DEMs). In particular, peak

Fig. 1 Photographs of the **a**) sector of the northern slope of Mt. Pendolo hit by wildfire in August 2024 and **b**), **c**), **d**) buildings involved in the debris flood

discharge was estimated using the soil conservation service curve number (SCS-CN) method (USDA-SCS, 1972) that was originally calibrated for catchments in the USA but has been applied in many agricultural and urban catchments worldwide, including in the peri-Vesuvian area of southern Italy (De Paola et al. 2013; Reder et al. 2015; Violante et al. 2016). Our results provide a better understanding of slope-scale susceptibility to postwildfire debris floods on Mt. Pendolo and in the whole peri-Vesuvian area of southern Italy.

Geologic, geomorphologic, and climatic settings

On September 11, 2024, a debris flood developed along the northeastern slope of Mt. Pendolo in the Gragnano municipality (Fig. 2a). With a maximum elevation of 618 m above sea level (asl), this relief is located in the northern sector of the Lattari Mts. in the Campania region and is dominated by a NW–SE-trending carbonate ridge. Its formation is related to the Miocene compressive tectonism that drove the development of the Sarno, Avella, and Lattari Mountains (D'Argenio et al. 1973; Mostardini and Merlini 1986; Patacca and Scandone 2007). The calcareous strata dipping 35–40° toward the SW commonly produces outcrops at high elevations that form local subvertical cliffs along the slopes. A Mio-Pliocene paleosurface bordered by NW–SE and NE–SW normal faults characterizes the top of the relief. The carbonate bedrock of Mt. Pendolo is covered by pumices and pyroclastic soils from the AD 79 explosive eruption of the Somma–Vesuvius and is overlapped by deposits derived from pedogenic processes (Fig. 2a). Coarse white and gray pumices form an in-place pyroclastic cover with a thickness ranging from 0 to 4.0 m that increases from higher to lower elevations and from steeper to flatter areas (Fig. 2a) and reflects the geomorphological heterogeneity of the slope (Lucà et al. 2014).

The northeastern slope of Mt. Pendolo is 30–35° steep and presents a rectilinear-concave shape up to higher altitudes, where subvertical morphologies are observable. High-relief energy and tectonic processes have been responsible for the torrential regime of the hydrographic network. In particular, this network is characterized by a low hierarchical degree and deeply incised gullies that are responsible for the small fans located at the footslope. The two catchments that supported the development of the September 11, 2024, event extend for 0.075 km^2 and 0.041 km^2 and have maximum elevations of 579 and 520 m asl, respectively. The catchments have Melton ratios (watershed relief divided by the square root of the watershed area; Melton 1957) > 0.60, which is typical of debris flow-dominated watersheds (Ilinca 2021). As documented previously, debris flows have occurred along the northeastern slope of Mt. Pendolo historically and recently (e.g., Mele and Del Prete 1999; de Riso et al. 2004; Di Crescenzo et al. 2008). Typically, such events initiate as shallow translational (or rotational) debris slides and subsequently evolve into rapid debris avalanches/debris flows. The term "debris flow" is used to describe these events because it represents the dominant propagation mechanism (Hungr et al. 2014). The detachment zone has a limited extent (a few m^2), but the initial mobilized volume generally increases with the entrainment of sediments and vegetation into the moving flow. Figure 2b shows the main events that occurred along the northeastern slope of Mt. Pendolo from 1764 to 1997, as well as some updated events (from Fusco et al. 2023).

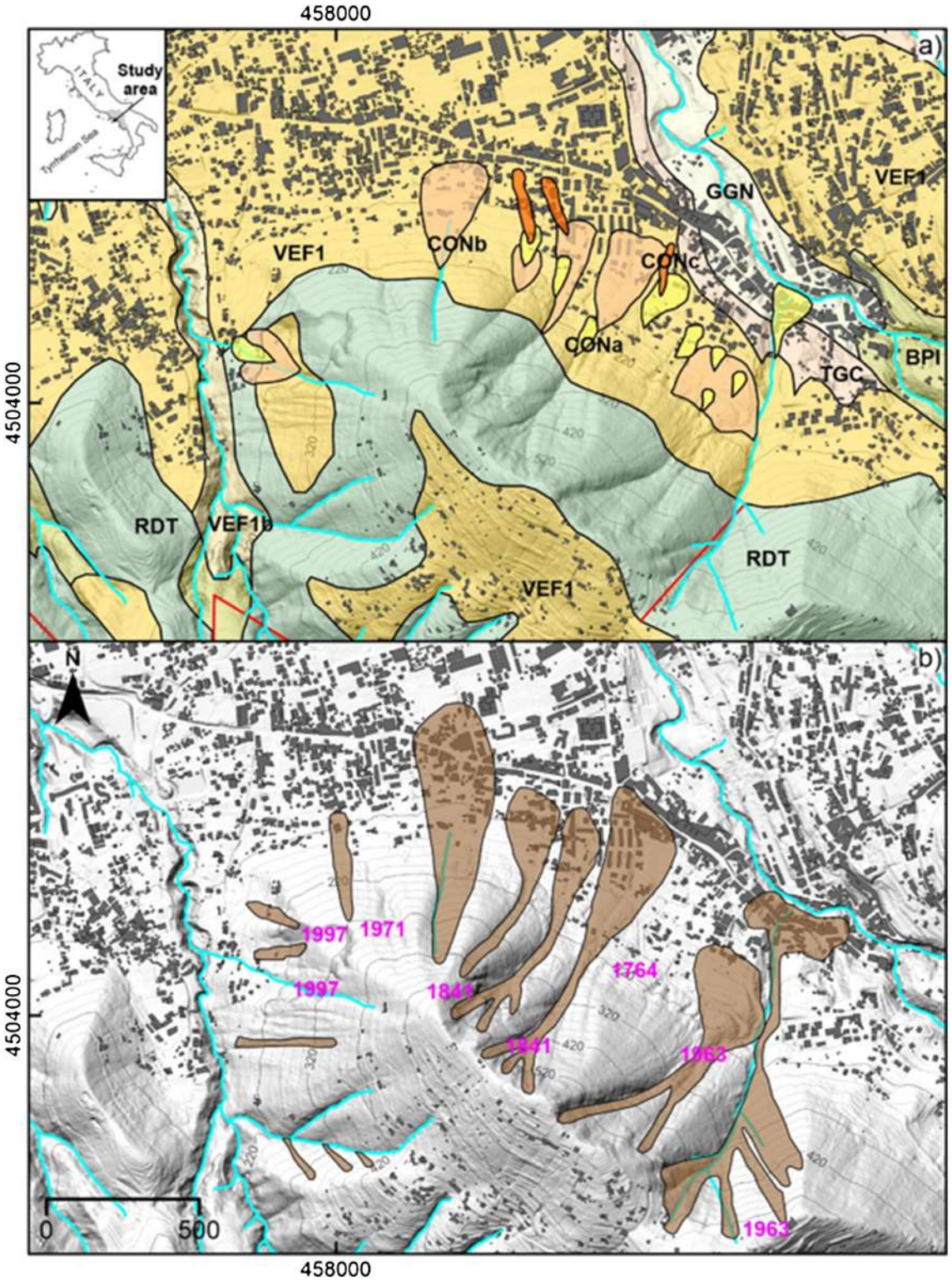

Fig. 2 **a** Geological map derived from CARG Project Sheets 466 and 485 Sorrento and Termini (https://www.isprambiente.gov.it/Media/carg/466_485_SORRENTO_TERMINI/Foglio.html), and **b** landslide inventory map of the study area. Legend: VEF1, Vesuvian Phlegraen Formation; VEF1b, Scanzano Formation; TGC, Campanian Ignimbrite; GGN, Gragnano Formation; BPI, Pimonte Formation; RDT, Radiolitic carbonate series; CONa, historic fan deposits; CONb, Olocenic fan deposits; and CONc, remaining likely historic fan

The last event occurred on January 10, 1997; it had an average length of 220 m and involved 4500 m^3 of material (Di Crescenzo and Santo, 1999; de Riso et al. 2004).

The thermopluviometric regime of the area is modulated by strong seasonality and presents the typical features of a Mediterranean climate (Crespi et al. 2018). Despite its proximity to the coast, Mt. Pendolo receives average rainfall that is comparable to several inland Apennine reliefs, which are the wettest sites in the Campania region. According to data provided by the Campania region Civil Protection (http://centrofunzionale.regione.campania.it/#/pages/sensori/archivio-pluviometrici, last access on 03/10/2024), average precipitation in the study area was approximately 1400 mm/year from 2002 to 2021. The monthly and seasonal precipitation amounts follow a bimodal distribution with two peaks. The first peak occurs in autumn (560 mm/year), and the second peak occurs in winter (530 mm/year). The minimum amount of precipitation occurs in summer (150 mm/year). Rainfall is characterized by pronounced interannual variability on yearly and seasonal time scales. For example, 2000–2100 mm of rain was observed in 2010 and 2013 (the wettest of the last two 10-year periods), whereas slightly more than 1000 mm of rain was recorded in 2006 and 2020. Recent work by Capozzi et al. (2023a) highlighted the meteorological scenarios that are behind the most relevant rainfall episodes in the Campania region. In general, heavy precipitation in this area is the result of a nontrivial linkage between synoptic forcing, mesoscale mechanisms (such as low-level wind convergence lines), and orographic features. In coastal areas during autumn, the very warm surface temperature of the Tyrrhenian Sea further contributes to the development of convective precipitation systems.

Wildfire extent and severity

The extent of the wildfire was estimated with a normalized burning ratio (NBR) (Roy et al. 2006). This index uses near-infrared (NIR) and shortwave infrared (SWIR) bands to derive products suitable for the identification of burned areas. Healthy vegetation exhibits high reflectance in the NIR band and low reflectance in the SWIR band, and burned areas exhibit high reflectance in the SWIR band and low reflectance in the NIR band. The NBR index can be calculated according to the following formula:

$$NBR = (NIR - SWIR)/(NIR + SWIR) \quad (1)$$

where NIR and SWIR correspond to the bottom of the atmosphere (BoA) reflectance in the NIR and SWIR bands, respectively. For this analysis, prewildfire and postwildfire multispectral Sentinel-2 imagery were acquired on August 09, 2024, and August 14, 2024. Each image was used for calculating the NBR using the B08 band, which corresponded to NIR, and the B12 band, which corresponded to SWIR2. The prewildfire and postwildfire NBR values were used to identify the extent and severity of the wildfire (Keeley 2009) by comparing prewildfire and postwildfire conditions (i.e., dNBR; Miller and Thode 2007). More specifically, while the extent of the wildfire was identified from dNBR values higher than 0.099, dNBR values between 0.1 and 0.265 indicated a low severity burn, values between 0.27 and 0.43 indicated a moderate severity burn, and values between 0.44 and 0.65 indicated a moderate–high severity burn. Values higher than 0.66 corresponded to high burn severity.

From the perspective of landslide development, the importance of estimating burn severity is related to the ability of wildfires to alter the hydrologic response of a drainage basin by reducing rainfall infiltration and increasing surface runoff (Parise and Cannon 2012). This is caused by the (i) removal of soil-mantling vegetation and litter, (ii) deposition of ash, (iii) changes in the physical properties of the soil and rock, and (iv) enhancement, generation, or destruction of water-repellent soils. These changes also affect the aptitude of soils to be eroded and availability of sediment for mobilization by water flow (Moody and Martin 2001). Consequently, a combination of sediment-laden flows and debris flows or/and debris floods can occur after a wildfire (Cannon 2001; Wieczorek et al. 2001).

Figure 3 depicts the analysis of burn extent and severity. Overall, the extent of the wildfire was ~ 0.13 km^2, and this extent corresponds to the area of the map with burn severity higher than 0.99. This area stretched across two adjacent catchments, the first of which (the western catchment) was completely affected by the wildfire and the second of which (the eastern catchment) was partially affected in its middle and upper sectors. The burn severity in areas affected by the wildfire ranged from low to moderate–high. No areas with high burn severity were recognized using this approach. As expected, the low-severity areas were located at the margin of the burned area, and the moderate and moderate–high severity regions were located completely inside the burned area. The moderate severity burned area covered ~ 0.05 km^2, and the moderate–high severity burned area covered ~ 0.04 km^2.

Storm characteristics

In the evening of September 11, 2024, the study area was affected by a convective precipitation episode. To reconstruct the precipitation field at ground level, rain gauge and weather radar observations were employed. The in situ data were provided by three stations belonging to the Campania Region Civil Protection network (https://centrofunzionale.regione.campania.it/#/pages/sensori/sensor-utility, last access on 27/09/2024): Gragnano (40.68652778°N, 14.5263889°E, 185 m asl), Lettere (40.70355556°N, 14.53202778°E, 291 m asl), and Pimonte (40.67338889°N, 14.50397222°E, 438 m asl). The rainfall data collected by these stations were available with a temporal resolution of 10 min. In addition, the observational dataset included horizontal reflectivity measurements (hereafter, Z) acquired by X-band weather radar operating in the Naples urban area at the top of Castel Sant'Elmo (40.8433°N, 14.2385°E, 280 m asl). This radar, managed by the Parthenope University of Naples, is a single-polarization system that scans the atmosphere every 10 min at eight elevations (1, 2, 3, 4, 5, 7.5, 10, and 12.5°), with a range resolution of 450 m and an azimuth resolution of 1.0°. After careful quality control to remove and mitigate several systematic errors (Capozzi et al. 2022), the reflectivity volumes were processed to retrieve the vertical maximum intensity (hereafter, VMI), which represents the maximum reflectivity value in each quasivertical atmospheric column sampled by the weather radar. The VMI product, which was originally in native spherical coordinates, was remapped into a two-dimensional regular Cartesian grid with a horizontal resolution of 500 × 500 m (see Capozzi et al. 2022 for methodological details about WR-10X radar data processing). Figure 4a shows the locations of the gauges and weather radar. Notably, the Mt. Pendolo area is effectively monitored by WR-10X at all antenna elevation angles,

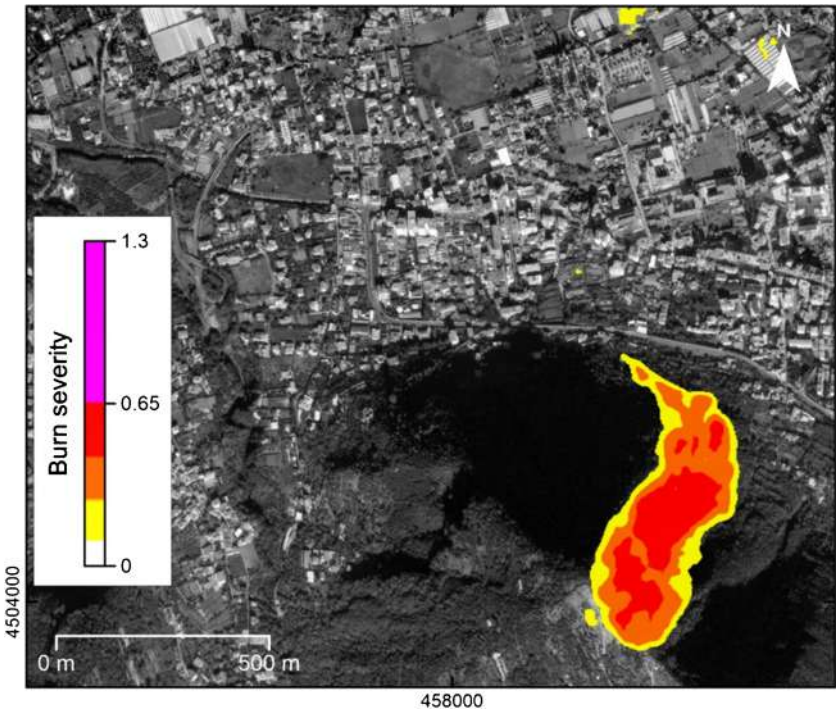

Fig. 3 Results from the burn severity analysis based on Sentinel-2 imagery and the NBR index. Yellow to red areas experienced moderate to high burn severity (Keeley 2009). UTM 33 N coordinates are shown at the map edges

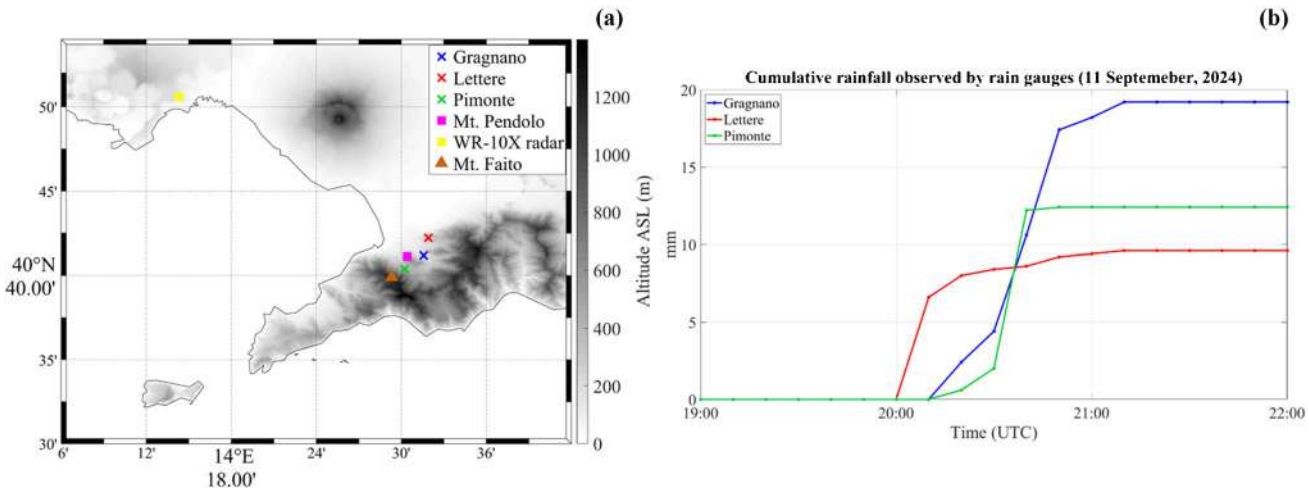

Fig. 4 **a**) A map of the study area, with the locations of the rain gauges (Gragnano, blue cross; Lettere, red cross; and Pimonte, green cross) and the WR-10X weather radar (filled-in yellow square). In addition, the locations of Mt. Pendolo and Mt. Faito are indicated as a magenta filled-in square and a brown filled-in triangle, respectively. **b**) A 10-min time series of cumulative rainfall (mm) registered by the three rain gauges on September 11, 2024, from 19:00 to 22:00 UTC. The rain gauges are color-coded as in **a**)

although the surrounding complex topography of the Lattari Mts. may introduce some impairments in the characterization of convective storms (in several azimuthal directions, the radar beam at the 1° antenna elevation angle is almost completely shielded by mountains).

Prior to September 11, 2024, the study area was affected by two distinct cyclonic circulations. The first low-pressure area hit the Campania region on September 9 and caused convective precipitation events, especially during the morning. Rainfall totals ranged between 25.2 mm in Gragnano and 28.8 mm in Pimonte. On September 10, a short-lived rainfall episode occurred during the night and produced between 2.0 mm in Gragnano and 4.2 mm in Lettere. During the evening of September 11, the synoptic-scale scenario was modulated at mid-tropospheric levels by a trough extending

from the Scandinavian Peninsula to Central Europe that gradually approached the Mediterranean area. On the Italian Peninsula, the sea level pressure field was characterized by a cyclonic area over northern Italy, which drove a weak western flow over the study area. This large-scale setup resulted in a moderately unstable environment over Campania that supported the development of isolated convective cells (Capozzi et al. 2023b).

Figure 4b presents the time series for cumulative rainfall registered at the three rain gauges. A close inspection of this figure reveals relevant differences among the stations in precipitation intensity, amount, and temporal evolution, which can be considered typical of convective events. More specifically, in Lettere (red line), rain started falling between 20:00 and 20:10 UTC, during which time a total of 6.8 mm was recorded. Subsequently, moderate to light rain was registered until 21:10 UTC. The total cumulative rainfall was 9.6 mm at this station. The Gragnano (blue line) and Pimonte (green line) stations experienced a similar pattern of rainfall, although with quantitative differences. At both stations, precipitation began between 20:10 and 20:20 UTC. In Pimonte, heavy rainfall occurred between 20:30 and 20:40 UTC, and the rain gauge reported a total of 10.2 mm. The event lasted until 20:50 UTC and a total of 12.4 mm of rain was recorded. In Gragnano, heavy rainfall was observed from 20:30 to 20:50 UTC, and the accumulated precipitation was 13.0 mm. This main phase was followed by light rain from 20:50 to 21:10 UTC. The total accumulated rainfall was 19.6 mm.

The WR-10X radar scans provide additional insights into the spatiotemporal evolution of the precipitation event. Importantly, the radar-based rain rate (RR) estimates were obtained from the VMI product using the following equation:

$$RR = \left(10^{\frac{VMI}{10}}\right)^{\frac{1}{b}} \frac{1}{a} \quad (2)$$

The regression coefficients were set to $a = 134.0$ and $b = 1.55$ following Maki et al. (2005). Figure 5 shows the RR field estimated by weather radar at three different times: 19:50 UTC (a), 20:20 UTC (b), and 21:00 UTC (c). The convective precipitation event left the first signature on the WR-10X radar images at 19:50 UTC (Fig. 5a). During this stage, the rain cell was located just west of Mt. Pendolo and it extended downstream from Mt. Faito on a southwestern to northeastern axis. The precipitation system subsequently widened its range of action, and at 20:20 UTC it also affected the area of Mt. Pendolo. However, as revealed by Fig. 5b, the main rainfall core, which was characterized by RR values of up to 60 mm h^{-1}, was a few kilometers south of the study area. At 20:30 UTC, the convective phenomenon changed shape and exhibited a northwestern to southeastern orientation with a main precipitation core that was very close to Mt. Pendolo, where RR

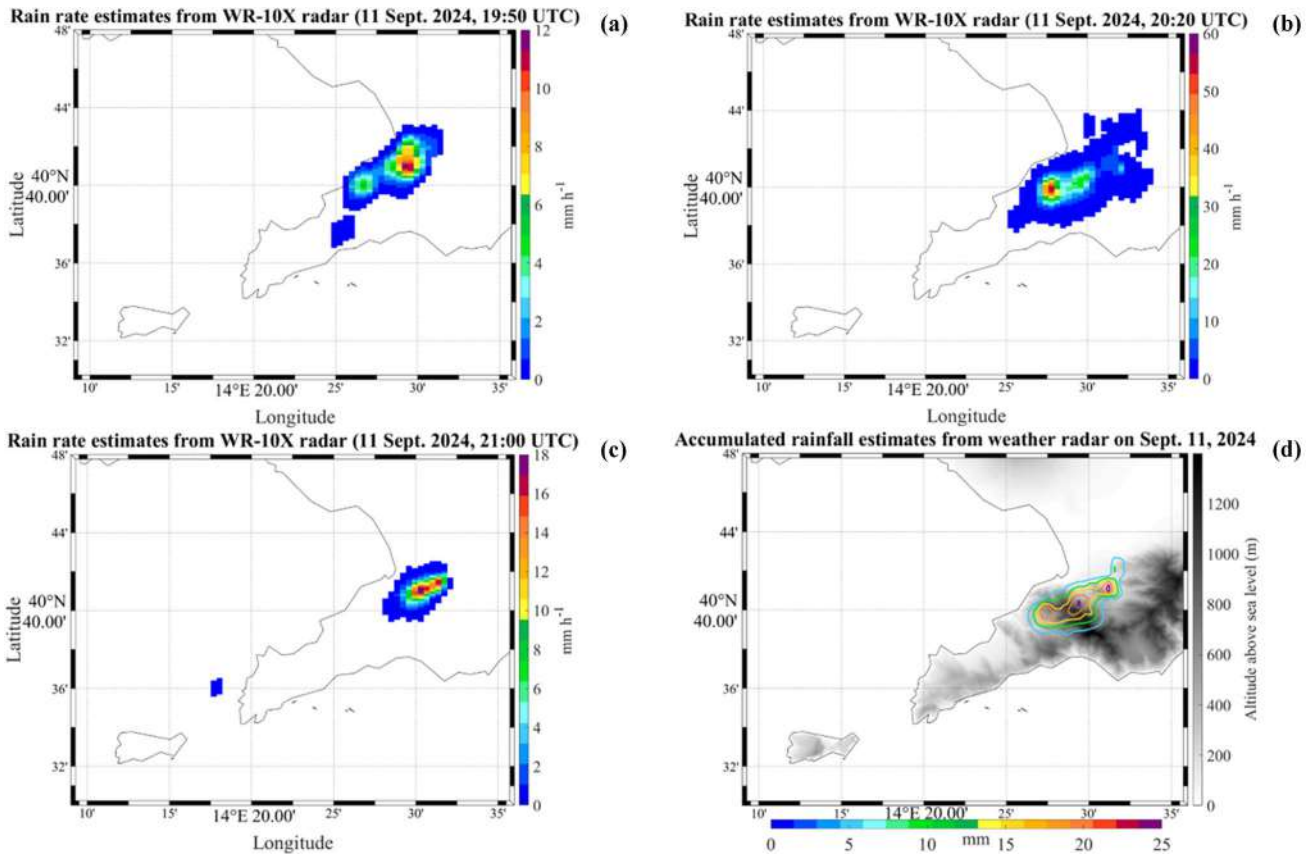

Fig. 5 Rain rate field (in mm $h.^{-1}$) estimated from WR-10X on September 11, 2024, at 19:50 UTC (**a**), 20:20 UTC (**b**), and 22:00 UTC (**c**). **d** The total accumulated rainfall field (in mm) computed from the WR-10X radar scans collected during the entire precipitation event (from 19:50 to 22:20 UTC)

values of up to 40–50 mm h^{-1} were detected. From 21:00 UTC, a gradual weakening of rain intensity was observed along with a reduction in rain cell extension. At this time, according to Fig. 5c, the RR values were lower than 20 mm h^{-1}. After 21:20 UTC, no relevant radar echoes were detected in the study area. Figure 5d presents the total accumulated rainfall field estimated by WR-10X over the study area. Three spatial peaks in rainfall, with similar magnitudes, were easily detected. The first two were located over Mt. Faito and the third was in proximity to Mt. Pendolo. In such areas, accumulated rainfall of up to 25 mm was observed. Precipitation decreased along a gradient moving from the main cores to the northwestern and southeastern directions.

According to our analysis of the WR-10X radar data, the meteorological event responsible for the debris flood that occurred at Gragnano can be defined as an isolated orographic-induced convective system, which developed over the Lattari Mts. and then propagated downstream into a moderately unstable environment characterized by relatively weak winds, especially at the middle and upper tropospheric levels.

To assess the severity of the rainfall event, a return period calculation was carried out. Following World Meteorological Organization recommendations (WMO, 2009), the well-known Gumbel extreme value distribution (Gumbel 1941) was applied to estimate the return period of maximum rainfall amounts. Our analysis of storm characteristics revealed that the Gragnano rain gauge recorded the highest total accumulated rainfall amount among the stations. In addition, the rainfall measured at this station was close to that estimated for the Mt. Pendolo area (24.7 mm) from weather radar observations. For this reason, the return period analysis was based on Gragnano rainfall data. From the Campania Region Civil Protection database (https://centrofunzionale.regione.campania.it/#/pages/sensori/sensor-utility, last access on 04 December, 2024), we retrieved the subdaily (10-min resolution) time series of rainfall data collected at Gragnano in the last 20 years (2004–2023).

Using these historical data, a return period analysis based on the annual maximum cumulative rainfall at different aggregation times was performed. Figure 6 shows the rainfall probability curves for different durations (10, 20, 30, and 60 min). The black unfilled circles indicate the maximum rainfall observed in Gragnano on September 11, 2024, at 10 min (6.8 mm), 20 min (13.0 mm), 30 min (15.0 mm), and 60 min (19.6 mm). Based on these results, the rainfall event assessed in this study has a return period level of less than or equal to 1 year.

A return period calculation was also performed on a monthly basis, i.e., considering the year-by-year cumulative rainfall observed in September. However, the results were very similar: the return period of the September 11, 2024; rainfall event was 1.1 years at 10 min and 1.6 years at 20 min and 60 min. In addition, the return period of the highest 10 min rainfall recorded in Pimonte (10.2 mm at 20:40 UTC) was estimated. No relevant difference between Pimonte and Gragnano was detected: the return periods were 1.0 years on a yearly basis and 1.9 years on a monthly basis. Therefore, the convective system that hit the Mt. Pendolo area on September 11, 2024, produced a rainfall amount with a very short (≤ 1 year) return period. In addition, to better contextualize the magnitude of this event, we compared it with two previous significant rainfall episodes that affected the study area: January 10, 1997, and January 3, 1971. For both events, the rainfall records in Gragnano were provided by a station in the National Hydrographic and Mareographic Service network (http://www.bio.isprambiente.it/annalipdf/, last access on 08 January 2025), which managed hydrometeorological data collection in Italy from 1917 to 2002. The location of this station did not exactly coincide with that of the rain gauge in our analysis of the September 11, 2024, event. However, the two stations are close to each other and have similar altitudes, making them reasonably comparable. On January 10, 1997, the 24-h cumulative rainfall (which was the only information available) was 102.0 mm, whereas on January 3, 1971, the daily precipitation

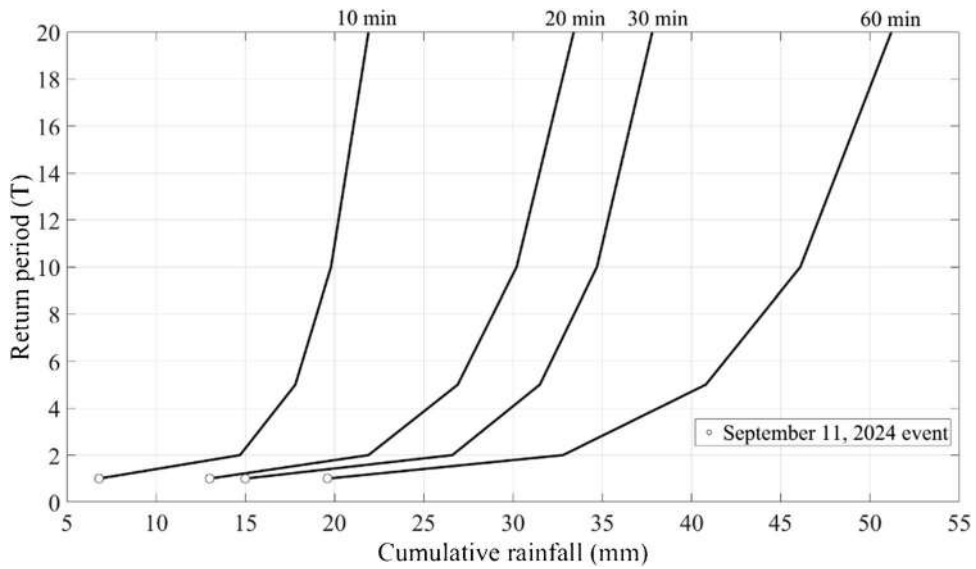

Fig. 6 Rainfall probability curves for different durations (10, 20, 30, and 60 min) resulting from the historical data recorded at the Gragnano monitoring station (40.68652778°N, 14.5263889°E). The black unfilled circles indicate the maximum rainfall accumulated at 10, 20, 30, and 60 min on September 11, 2024

was 65.5 mm. During the second event, a relevant rainfall episode also occurred on the previous day (January 2, 1971) during which the Gragnano station recorded 105.0 mm of precipitation. These cumulative rainfall amounts were much greater than the 19.6 mm observed on September 11, 2024, and were the result of meteorological dynamics typical of the cold season (the period from October to April). In both episodes, the study area was affected by a deep trough associated with a low-pressure area at the surface that moved from the western Mediterranean toward the Tyrrhenian Sea and caused long-lasting precipitation events that were enhanced by orographic lifting. This comparison with previous events corroborates our hypothesis that the ability of the September 11, 2024, event to trigger a debris flood was linked to increased runoff caused by the preceding wildfire.

Debris flood source and inundation areas

The source of the debris flood was identified via field observations, which were supported by unmanned aerial vehicle (UAV)-aided photography, DEMs, and satellite imagery interpretation in a GIS environment. The source area was considered to be the area supplying water and sediment to the channel; hence, field observations, DEMs, and interpretations of satellite imagery were oriented to identify areas in which runoff features developed, pyroclastic deposits were removed by the event itself, and/or landslide scars could be identified. Ground-based field observations were conducted on the lower and middle sectors of the slope that were accessible by hiking trails, and UAV-aided oblique photographs were taken along the middle and upper sectors of the slope to capture both the eastern and western catchments that contributed to the debris flood.

The inundation area was identified via field observations that were conducted a few to 10 days after the event in conjunction with pictures, videos, and eyewitness observations. Field observations of debris flood deposits and signatures of flow movement and impact (i.e., splash) on settlements were recorded during three field campaigns in the form of pictures and notes. Each picture or note was associated with X and Y UTM 33 N coordinates, which provided point localization. Similarly, for locations where the sediment had been removed during the emergency response and was not visible during field campaigns, online pictures and videos were compared with freely available Google Street View virtual paths to derive coordinates of significant points of debris flood propagation. Additional observations from eyewitness, regarding road segments that were involved in the debris flood, were also considered. All of the collected data were subsequently interpreted to reconstruct the overall inundation area, which was limited to the area where the solid fraction of the flow was significant.

Figure 7 shows the source and inundation areas that were identified for the September 11, 2024, event. The major sources of surface runoff generation were the eastern and western adjacent headwater

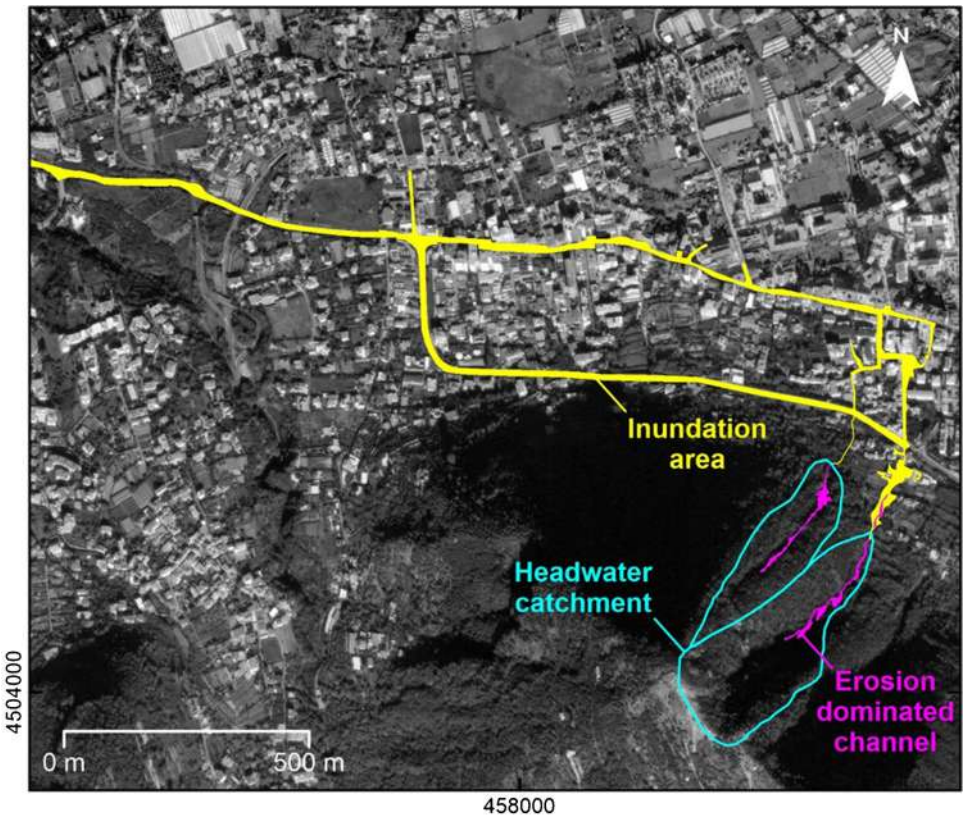

Fig. 7 Map showing the position and extent of the headwater catchment, erosion-dominated channel segment with major secondary landslide boundaries (i.e., magenta polygon), and inundation area in the September 11, 2024, debris flood. UTM 33 N coordinates are shown at map edges

catchments of 0.041 and 0.075 km² that were characterized by average slope angles of 37° and 41°, respectively. While the western catchment burned completely during the wildfire on August 11, 2024, only the upper sector of the eastern catchment was affected by the wildfire. Field observations indicated that many decimeter-wide runoff channels formed in the middle and lower sectors of the catchments, which concentrated runoff toward the channel. Within the lower sector of each catchment, erosion-dominated channels of approximately 250 m and 400 m occurred. In both cases, the channel beds appeared to be shaped in the carbonate bedrock, and landslide scars and remnants of sediment mobilized during the event were located along the right flanks of the channels. Lateral landslides observed along the channel of the western headwater catchment were generally smaller (in terms of area and volume) and located at lower elevations than those observed along the channel of the eastern catchment. The inundation area along which the pumice flow propagated during the event corresponded mostly to major roads and extended for 0.05 km². While both catchments contributed to the development of the debris flood, the inundation area was better developed in the eastern catchment, where fan-shaped deposits were observed. This finding was consistent with eyewitness data and indicates that the eastern catchment contributed to a significant fraction of the total flow. Multiple sediment pulses were also observed during the event. The first pulse consisted of a sediment-laden flow derived from a mixture of clear water and potentially ash produced by the wildfire. A second and more significant pulse represented the debris flood event. Data on the duration of each pulse were not available.

Estimating the sediment budget and peak discharge

The sediment volume mobilized during the debris flood was estimated with a DEM of difference (DoD) obtained using a preevent high-resolution (1-m single-sided pixel dimension) LiDAR-derived DEM and a postevent high-resolution (0.5-m single-sided-pixel dimension) LiDAR-derived DEM that were obtained on September 26, 2024. The preevent DEM, developed from LiDAR data acquired in 2020, was downloaded from the source at http://www.pcn.minambiente.it. The postevent LiDAR data were acquired during two consecutive DJI Matrice 300 RTK-based acquisitions. The UAV was equipped with a LiDAR L1 sensor. The first acquisition was completed by flying at a relative elevation of 120 m over the entire headwater catchment that contributed to the development of the debris flood and supplied both water and sediment. At this elevation, the LiDAR L1 sensor ensured a vertical resolution of the data slightly greater than 10 cm, which is good resolution for DEM-based differential analysis and volume estimation. The second acquisition was completed by flying at a relative elevation of 90 m along the lower channel segment of both catchments. The acquired multiecho LiDAR data were filtered and merged to create a minimum value DEM representative of the postevent catchment and channel topography. Preevent and postevent DEMs were used to create a DoD, which was used for gross volume estimation with the volume-between-surface method. Field observations and orthophoto (generated by a UAV) interpretation were used to map the erosion-dominated channel segments and lateral landslides that supplied sediment during the event. Field data depicting the local thickness of pyroclastic deposits before the event and changes in elevation were also considered when validating the estimation. In addition, the accuracy of the volume estimation was evaluated by computing the root mean square deviation (RMSD) of surface elevation for an area in which no change occurred between 2020 and 2024. For this area, a segment of the road following the base of the slope was considered (partially depicted by the dark gray polygon at the upper right edge of Fig. 8). To supplement the estimation of the net volume of sediment involved in the event, several samples of pumices that formed the pyroclastic cover were taken from the lateral landslides identified along the eastern channel. A physical characterization of the samples was carried out by means of particle size analysis according to ASTM D422.

The peak discharge during the debris flood was estimated using radar-based cumulative rainfall and morphometric catchment parameters via a water synthetic unit hydrograph reconstruction with the SCS-CN method (USDA-SCS, 1972). This method, which assumes a constant intensity and spatially uniform rainfall over the entire investigated area (e.g., Tufano et al. 2023), is based on the following balance equation:

$$\frac{P - I_a - Q}{S} = \frac{Q}{P - I_a} \tag{3}$$

where P is the total cumulative rainfall (mm), I_a is the initial abstraction (mm), Q is the runoff (mm), and S is the potential maximum soil moisture retention after runoff begins (mm). The total rainfall amount P was estimated from the available 10-min time series of radar-based cumulative precipitation estimates. More specifically, from the two-dimensional regular Cartesian radar grid, the pixels located within 1.5 km from Mt. Pendolo were taken into account. Among these pixels, the pixel with the highest rainfall amount was selected. This approach reduces underestimation of the surface rain field due to the increasing height of the sampled atmospheric volume with increasing distance from the radar site. The total rainfall P was obtained by integrating the selected 10-min cumulative rainfall estimates over time. With respect to runoff, the equation is as follows:

$$Q = \frac{(P - I_a)^2}{(P - I_a) + S} \tag{4}$$

This equation was used to predict Q with only a few input variables. Further simplifications of the SCS-CN method included considering the average value for I_a, which was set equal to 0.05 S, because the initial abstraction was considerably reduced by the absence of vegetation due to the wildfire, and the introduction of a parameter called the curve number CN, which allowed the estimation of S as follows:

$$S = \left(\frac{100}{CN} - 10\right) \tag{5}$$

CN varies between 30 for low runoff potential (and high infiltration) and 100 for high runoff potential, and it depends on land use, hydrologic soil group, hydrologic condition, and antecedent moisture conditions (USDA-SCS 1972). Considering the soil type based on the land use class and an aggravating factor related to fire severity, a value of CN equal to 92 was estimated for postfire conditions. This CN was calibrated by Guerriero et al. (2024) for

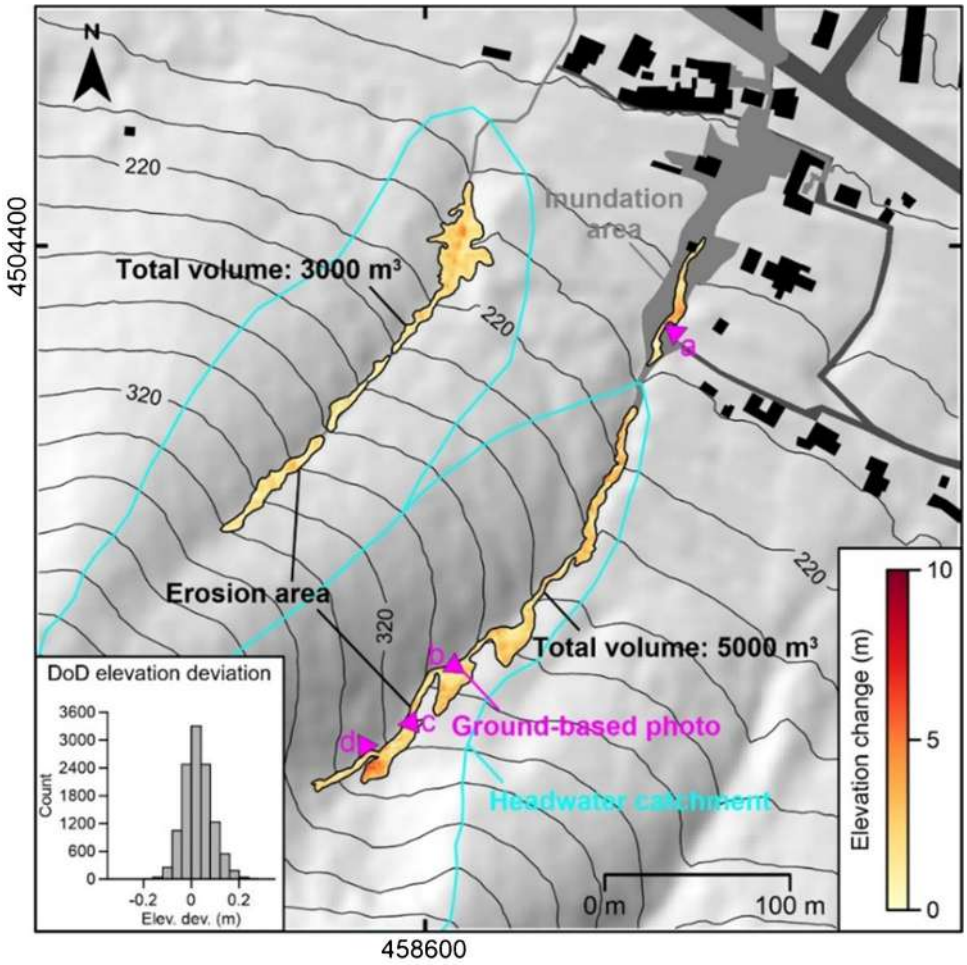

Fig. 8 Map showing the elevation changes over erosion-dominated channel segments identified in the headwater catchments that sustained debris flood development, the estimated total sediment volume, and the gross volume of the event. Lateral landslides and channel segments that contributed to the sediment budget of the event (i.e., magenta polygons) are located along the upper right flank of the eastern channel and along both flanks of the lower sector of the western channel. The red symbols indicate the locations of the ground-based photographs in Fig. 9

a small catchment in the Abruzzo region that experienced a wildfire and the development of a debris flood.

The synthetic unit hydrograph, defined as the ratio of runoff to peak discharge and the ratio of the duration of rainfall to the peak time, was estimated for both catchments. The water synthetic unit hydrographs were simplified as triangular, and, considering the limited size of the catchments, timing parameters were evaluated with the SCS lag equation. In particular, the ascending and descending phases, accounting for a specific duration, are represented by the accumulation time t_a. The peak discharge Q_p, modulated by the catchment area A and the net rainfall P_n, was obtained with the following equation:

$$Q_p = \frac{0.208 \cdot A \cdot P_n}{t_a} \quad (6)$$

T_a depends on the lag time and the concentration time of the catchment, which was estimated via the SCS formulation. Synthetic unit hydrographs were finally used to develop water runoff hydrographs on the basis of cumulative rainfall.

Figure 8 shows the shape and extent of erosion-dominated channel segments derived from the DoD and elevation changes that occurred between 2020 and 2024, which were partially due to the debris flood that occurred on September 11, 2024. The change in elevation along the channel developed within the western catchment between a few decimeters and 5 m. Within the eastern catchment, the maximum change in elevation was slightly greater than 6 m. Overall, while minimum values can be observed along the axis of existing channels, the maximum change in elevation occurred in the area of the landslide detachments.

The total erosion volume was estimated to be ~ 8000 m³. Along both channel segments, multiple landslides involving pumice pyroclastic deposits contributed to the sediment budget of the September 11, 2024, event (Fig. 9), and the gross volume of sediment involved in the event was estimated to be ~ 4100 m³. These

Fig. 9 Ground-based photographs depicting **a**) a channel segment in the eastern catchment dominated by erosion; **b**), **c**), **d**) scarps of lateral landslides

estimations were made with the volume between surface method and rely upon field observations of channel segments and slope sectors that contributed to the event. Further zones included in the erosion-dominated channel segment (black polygons) were excluded on the basis of field observations that indicated the absence of recent sediment removal. The sediment from these areas was likely removed during previous ordinary erosion events that developed along the channel between 2020 and 2023. In addition, the elevation precision of the postevent DEM, in comparison with the available preevent LiDAR DEM, indicated an RMSD of ± 0.065 m and a distribution of residuals, as depicted in the inset graph in Fig. 8. Extrapolating to the total gross volume *n* indicated a volume accuracy of ± 110 m^3.

The particle size analysis of samples taken at the channel margin indicated that the sediment consisted mainly of gravel with sand percentages between 3 and 17% (Fig. 10). On the basis of the grain

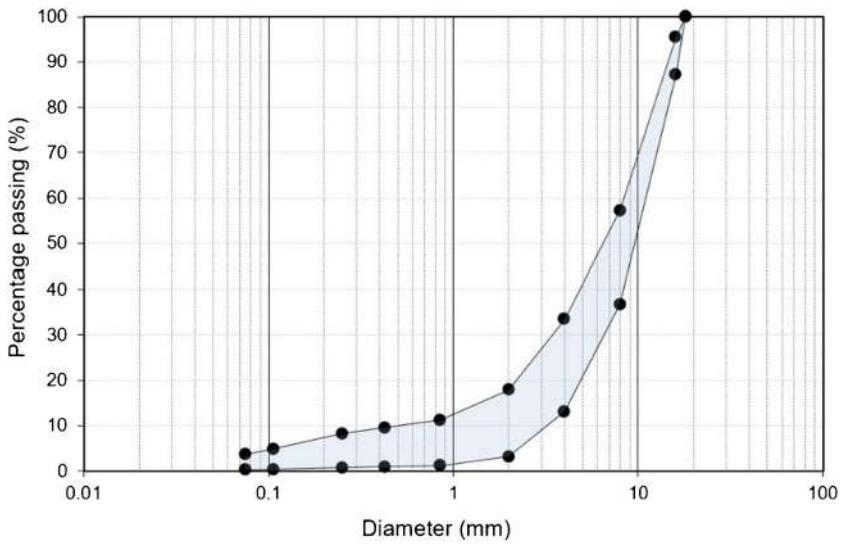

Fig. 10 Granulometric spindles for the analyzed samples

size spindle, the intergranular porosity varied between 30 and 40% (Esposito and Guadagno 1998; Sepe et al. 2023b). The presence of voids within pyroclastic materials must be considered when the net solid fraction is estimated, and a more reliable estimate of the total sediment volume would be between ~ 2450 and ~ 2850 m^3. In this estimate, the contribution of the ash produced by the wildfire cannot be considered.

Concentration times of approximately 5 min were estimated for both catchments, which indicated a very rapid runoff in the entire drainage area. As a result, the cumulative triggering rainfall of 24.7 mm in 80 min (for a maximum intensity of 6.6 mm/10 min) resulted in peak discharge values of 2.8 and 1.5 m^3/s for the eastern and western catchments, respectively (Fig. 11). By considering the estimated sediment budget that was potentially mobilized by the event and assuming a proportional relationship between the conveyed volume and water discharge distribution, we estimated the peak discharge of the debris flood. As shown in Fig. 11, the peak discharges increased to 4.6 m^3/s for the eastern catchment and 2.7 m^3/s for the western catchment, and the water fraction accounted for approximately 40% of the total.

Conclusions

The September 11, 2024, debris flood that hit the urban area of Gragnano, in the province of Naples, southern Italy, was triggered 1 month after a wildfire affected two headwater catchments. Wildfire severity in the catchments ranged from moderate to moderate–high. The catchment areas that sustained debris flood development were 0.041 and 0.075 km^2 and had average slope angles of 37° and 41°. The convective precipitation event that triggered the debris flood produced a total rainfall of 24.7 mm over a duration of 80 min, with a maximum intensity of 6.6 mm/10 min. The sediment involved in the event was formed largely by pumices, which consisted of gravel with a limited sand fraction, and the inundation area corresponded to major roads and extended for 0.05 km^2. Total gross sediment volume entrained into the flow, mainly by landslides, was estimated to be ~ 4100 ± 110 m^3, and the mixture (water and sediment) peak discharge was estimated to be 4.6 m^3/s for the eastern catchment and 2.7 m^3/s for the western catchment. Sediment concentration was estimated to be approximately 0.6.

On the basis of these results, and considering that the morphometry of the catchments was typical of debris flow-dominated catchments, the debris flood likely developed due to the dilution of an initial debris flow by the sediment contribution of a number of landslides generated by rainfall and erosion. The western catchment contributed to the event through the development of a sediment-laden flow that also reached the urban area. The difference in the behavior of the contributing catchments was potentially related to the spatial distribution of available sediment. Indeed, while a significant amount of sediment was observed in the field in the eastern sector of the upper and middle portions of the eastern catchment, no significant amount of available sediment was observed in the upper and middle portions of the western catchment. This may be due to previous landslide events across the area. The triggering event was characterized by a limited amount of total rainfall and a limited intensity, and the subsequent debris flood was related to increased runoff following the preceding wildfire, an occurrence that has been widely documented in the scientific literature.

Our analysis and interpretation of the event and development process provide a basis for interpreting similar events in areas with pyroclastic deposits under postwildfire conditions, as the increased frequency of debris floods in the peri-Vesuvian area of Italy represents an emerging source of risk for people and settlements.

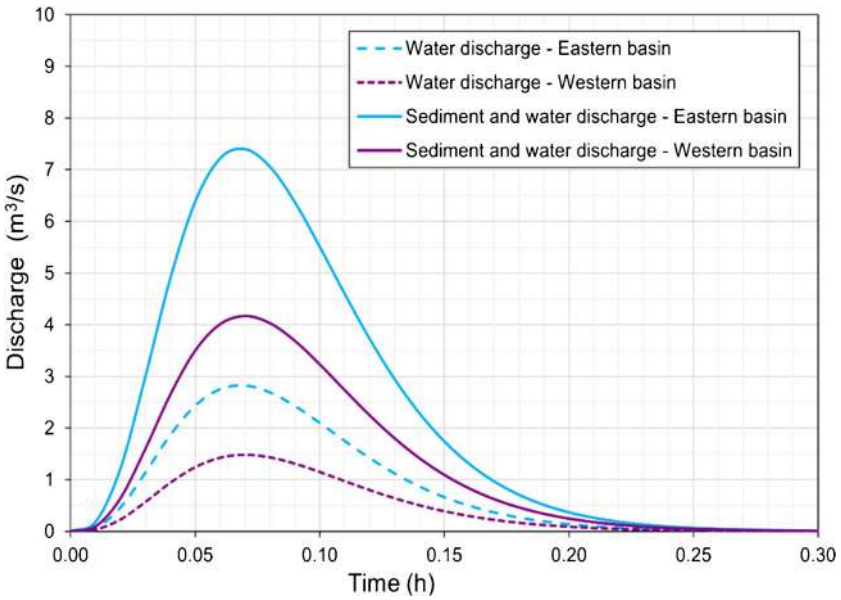

Fig. 11 Runoff hydrographs were estimated for the eastern and western catchments. The dashed lines indicate clear water discharge, and the continuous lines indicate the total flow discharge (water and sediment)

Acknowledgements

The authors thank the Gragnano Municipality for providing support during fieldwork and the Civil Protection of the Campania region (Multirisk Functional Centre) for providing rainfall data. The authors also thank the anonymous reviewer for providing constructive reviews of the manuscript.

Funding

Open access funding provided by Università degli Studi di Napoli Federico II within the CRUI-CARE Agreement. This study was carried out within the RETURN Extended Partnership and received funding from the European Union Next-GenerationEU (National Recovery and Resilience Plan – NRRP, Mission 4, Component 2, Investment 1.3 – D.D. 1243 2/8/2022, PE0000005, CUP: E63C22002000002).

Data availability

All data used in this work are either publicly available or available from the authors upon reasonable request.

Declarations

Competing interests The authors declare no competing interests.

References

Borga M, Stoffel M, Marchi L, Marra F, Jacob M (2014) Hydrogeomorphic response to extreme rainfall in headwater systems: flash floods and debris flows. J Hydrol 518:194–205

Calcaterra D, Parise M, Strumia S, Mazzella E (2007) Relations between fire, vegetation and landslides in the heavily populated metropolitan area of Naples, Italy. In: Proc. 1st North American Landslides Conference. Association of Environmental and Engineering Geologists. pp 1448–1461

Calcaterra D, Santo A (2004) The January 10, 1997 Pozzano landslide, Sorrento Peninsula. Italy Eng Geol 75(2):181–200

Cannon S (2001) Debris-flow generation from recently burned watersheds. Environ Eng Geosci 7:321–341

Cannon S, Powers P, Savage W (1998) Fire-related hyperconcentrated and debris flows on Storm King Mountain, Glenwood Springs, Colorado, USA. Environ Geol 35(2–3):210–218

Cannon S, Gartner J, Rupert M, Michael J, Rea A, Parrett C (2010) Predicting the probability and volume of post wildfire debris flows in the intermountain western United States. GSA Bull 122(1–2):127–144

Capozzi V, Mazzarella V, De Vivo C, Annella C, Greco A, Fusco G, Budillon GA (2022) Network of X-band meteorological radars to support the motorway system (Campania Region Meteorological Radar Network Project). Remote Sensing 14(9):2221. https://doi.org/10.3390/rs14092221

Capozzi V, Rocco A, Annella C, Cretella V, Fusco G, Budillon G (2023a) Signals of change in the Campania region rainfall regime: an analysis of extreme precipitation indices (2002–2021). Meteorol App 30(6):e2168

Capozzi V, Annella C, Budillon G (2023b) Classification of daily heavy precipitation patterns and associated synoptic types in the Campania Region (southern Italy). Atmos Res 289:106781. https://doi.org/10.1016/j.atmosres.2023.106781

Carabella C, Miccadei E, Paglia G, Sciarra N (2019) Post-wildfire landslide hazard assessment: the case of the 2017 Montagna Del Morrone fire (Central Apennines, Italy). Geosciences 9(4):175

Church M, Jakob M (2020) What is a debris flood? Water Resour Res 56(8):e2020WR027144

Crespi A, Brunetti M, Lentini G, Maugeri M (2018) 1961–1990 high-resolution monthly precipitation climatologies for Italy. Int J Climatol 38(2):878–895

D'Argenio B, Pescatore T, Scandone P (1973) Schema geologico dell'Appennino meridionale (Campania e Lucania). Atti del convegno "Moderne vedute sulla geologia dell'Appennino." Acc Naz Lincei 183:49–72

De Paola F, Ranucci A, Feo A (2013) Antecedent moisture condition (SCS) frequency assessment: a case study in southern Italy. Irrig Drain 62(S2):61–71

de Riso R, Budetta P, Calcaterra D, Santo A, Del Prete S, De Luca C, Di Crescenzo G, Guarino PM, Mele R, Palma B, Sgambati D (2004) Fenomeni di instabilità dei Monti Lattari e dell'area flegrea (Campania): scenari di suscettibilità da frana in aree-campione. Quaderni di Geologia Applicata 11(1):5–30

Di Crescenzo G, Santo A (1999) Analisi geomorfologica delle frane da scorrimento–colata rapida in depositi piroclastici della Penisola Sorrentina (Campania): Geomorphological analysis of the rapid earth flows in the pyroclastic deposits of the Surrentine Peninsula (Campania, Italy). Geografia Fisica e Dinamica Quaternaria 22(1):57–72

Di Crescenzo G, De Falco M, Iervolino VE, Rinaldi S, Santangelo N, Santo A (2008) Proposal of a new semiquantitative methodology for flowslides triggering susceptibility assessment in the carbonate slope contexts of Campania (Southern Italy). Ital J Eng Geol Environ 8(1):61–79

Esposito L, Guadagno F (1998) Some special geotechnical properties of pumice deposits. Bull Eng Geol Env 57:41–50. https://doi.org/10.1007/s100640050019

Forte G, Pirone M, Santo A, Nicotera MV, Urciuoli G (2019) Triggering and predisposing factors for flow-like landslides in pyroclastic soils: the case study of the Lattari Mts. (southern Italy). Eng Geol 257:105137

Fusco F, Tufano R, De Vita P, Di Martire D, Di Napoli M, Guerriero L, Mileti FA, Terribile F, Calcaterra D (2023) A revised landslide inventory of the Campania region (Italy). Scientific Data 10(1):355. https://doi.org/10.1038/s41597-023-02155-6

Gabet E, Bookter A (2008) A morphometric analysis of gullies scoured by post-fire progressively bulked debris flows in southwest Montana, USA. Geomorphology 96(3–4):298–309

Guerriero L, Guadagno FM, Revellino P (2019) Estimation of earth-slide displacement from GPS-based surface-structure geometry reconstruction: estimation of earth-slide displacement. Landslides 16:425–430. https://doi.org/10.1007/s10346-018-1091-0

Guerriero L, Francioni M, Calcaterra D, Di Martire D, Palumbo S, Zito C, Sciarra N (2024) Reduced complexity debris flow/flood hazard assessment at the southwestern slope of Mt. Omo, L'Aquila municipality, central Italy. Landslides 21(1):183–195

Gumbel EJ (1941) The return period of flood flows. Ann Math Stat 12:163–190

Hungr O, Leroueil S, Picarelli L (2014) The Varnes classification of landslide types, an update. Landslides 11(2):167–194

Ilinca V (2021) Using morphometrics to distinguish between debris flow, debris flood and flood (Southern Carpathians, Romania). CATENA 197:104982

Kean J, Staley D, Cannon S (2011) In situ measurements of post-fire debris flows in southern California: comparisons of the timing and magnitude of 24 debris-flow events with rainfall and soil moisture conditions. J Geophys Res Earth Surf 116:F03025

Keeley J (2009) Fire intensity, fire severity and burn severity: a brief review and suggested usage. Int J Wildland Fire 18(1):116–126

Lucà F, D'Ambrosio D, Robustelli G, Rongo R, Spataro W (2014) Integrating geomorphology, statistic and numerical simulations for landslide invasion hazard scenarios mapping: an example in the Sorrento Peninsula (Italy). Computer and Geosciences 67:163–172

Maki M, Iwanami K, Misumi R, Park SG, Moriwaki H, Maruyama KI, Watabe I, Lee D, Jang M, Kim H, Bringi VN, Uyeda H (2005) Semi-operational rainfall observations with X-band multi-parameter radar. Atmos Sci Lett 6(1):12–18

Mele R, Del Prete S (1999) Lo studio della franosità storica per la valutazione della pericolosità da frane. Un esempio dell'area di Gragnano (Campania). Boll Soc Geol Ital 118:91–111

Melton M A (1957) An analysis of the relation among elements of climate, surface properties and geomorphology. Technical Report No. 11, Columbia University

Miller J, Thode A (2007) Quantifying burn severity in a heterogeneous landscape with a relative version of the delta Normalized Burn Ratio (dNBR). Remote Sens Environ 109(1):66–80

Moody JA, Martin KJ (2001) Initial hydrologic and geomorphic response following a wildfire in the Colorado Front Range. Earth Surf Proc Land 26:1049–1070

Mostardini F, Merlini S (1986) Appennino centro-meridionale: sezioni geologiche e proposta di modello strutturale. In: Geologia dell'Italia centrale. Congresso nazionale 73:147–149

Parise M, Cannon S (2012) Wildfire impacts on the processes that generate debris flows in burned watersheds. Nat Hazards 61(1):217–227

Patacca E, Scandone P (2007) Geology of the Southern Apennines. Boll Soc Geol It (Ital J Geosci) Spec Issue 7:75–119

Reder A, Rianna G, Pagano L (2015) Approaches for estimating soil-atmosphere interaction fluxes in a pyroclastic cover. Advances in Environmental and Geological Science and Engineering, pp 273–280

Revellino P, Guerriero L, Grelle G, Hungr O, Fiorillo F, Esposito L, Guadagno FM (2013) Initiation and propagation of the 2005 debris avalanche at Nocera Inferiore (Southern Italy). Italian J Geosci 132(3):366–379. https://doi.org/10.3301/IJG.2013.02

Roy D, Boschetti L, Trigg SN (2006) Remote sensing of fire severity: assessing the performance of the normalized burn ratio. Remote Sens Environ 101(2):243–252

Santangelo N, Forte G, De Falco M, Chirico GB, Santo A (2021) New insights on rainfall triggering flow-like landslides and flash floods in Campania (Southern Italy). Landslides 18:2923–2933. https://doi.org/10.1007/s10346-021-01667-9

Sepe C, Calcaterra D, Di Martire D, Fusco F, Tufano R, Vitale E, Guerriero L (2023a) Triggering conditions and propagation of the December 2019 Palma Campania landslide: implications for residual hazard estimation at recurrent landslide sites. Eng Geol 322:107177. https://doi.org/10.1007/s11629-023-7955-3

Sepe C, Calcaterra D, Damiano E, Di Martire D, Greco R, Pappalardo L, Ramondini M, Vitale E, Russo G (2023b) Transient infiltration tests in pyroclastic soils with double porosity. J Mt Sci 20:3327–3342. https://doi.org/10.1007/s11629-023-7955-3

Staley D, Kean J, Cannon S, Schmidt K, Laber J (2013) Objective definition of rainfall intensity-duration thresholds for the initiation of post-fire debris flows in southern California. Landslides 10(5):547–562

Tufano R, Guerriero L, Annibali Corona M, Cianflone G, Di Martire D, Ietto F, Novellino A, Rispoli C, Zito C, Calcaterra D (2023) Multiscenario flood hazard assessment using probabilistic runoff hydrograph estimation and 2D hydrodynamic modelling. Nat Hazards 116:1029–1051. https://doi.org/10.1007/s11069-022-05710-3

USDA-SCS (1972) Hydrology, Section 4. In: National engineering handbook. Washington DC, USA

Violante C, Braca G, Esposito E, Tranfaglia G (2016) The 9 September 2010 torrential rain and flash flood in the Dragone catchment, Atrani, Amalfi Coast (southern Italy). Nat Hazards Earth Syst Sci 16:333–348. https://doi.org/10.5194/nhess-16-333-2016

Wieczorek GF et al (2001) Debris-flow and flooding hazards associated with the December 1999 storm in coastal Venezuela and strategies for mitigation. USGS Open-File Report, No. 144. https://doi.org/10.3133/ofr01144

WMO (2009) Manual on estimation of probable maximum precipitation. World Meteorological Organization, No. 1045

Luigi Guerriero · Rita Tufano (✉) · Chiara Di Muro · Lorenzo Esposito · Enza Vitale · Domenico Calcaterra
Department of Earth, Environmental and Resource Sciences, Federico II University of Naples, Naples, Italy
Email: rita.tufano@unina.it

Vincenzo Capozzi · Giorgio Budillon
Department of Science and Technology, University of Naples "Parthenope", Naples, Italy

Giovanni Forte
Department of Civil, Building and Environmental Engineering, Federico II University of Naples, Naples, Italy